J. Fluid Mech. (2026), *vol.* 1037, A36, doi:10.1017/jfm.2026.11677

JFM PAPERS

Confined gravity currents of non-Newtonian fluids with surface tension effects: experiments and comparison with theory

Sandro Longo[1], Marius Ungarish[2], Nicolò Merli[1], Seyedreza Hasheminejad[1], Vittorio Di Federico[3] and Luca Chiapponi[1]

[1]Department of Engineering and Architecture, Università degli Studi di Parma, Parco Area delle Scienze 181/A, Parma 43124, Italy

[2]Department of Computer Science, Technion, Haifa 320000, Israel

[3]Department of Civil, Chemical, Environmental, and Materials Engineering, Alma Mater Studiorum Università di Bologna, Viale Risorgimento 2, Bologna 40136, Italy

Corresponding author: Vittorio Di Federico, vittorio.difederico@unibo.it

(Received 16 September 2025 UTC; revised 26 March 2026 UTC; accepted 6 May 2026 UTC)

This study reports mainly experimental findings on the evolution of confined axisymmetric gravity currents of non-Newtonian fluids within a gap of fixed height, focusing on the combined effects of rheology and surface tension. The inflow rate follows a power-law dependence on time, with the exponent related to the fluid behaviour index. Prior theoretical work, validated against axisymmetric experiments with Newtonian fluids, has shown that (i) surface tension acting primarily at the grounding line can significantly modify the structure of classical self-similar solutions and (ii) the presence of a meniscus at the grounding line can be incorporated into the similarity formulation through a parameter relating its height to the gap thickness, thereby preserving self-similarity. Here, this framework is extended to non-Newtonian fluids, adopting a power-law rheology for analytical convenience, which is appropriate since the tested shear-thinning and shear-thickening fluids behave as power-law fluids over the relevant shear-rate range. The influence of surface tension is confirmed through twenty-one axisymmetric experiments using Newtonian and non-Newtonian fluids. Good agreement between theory and experiments is obtained only when the grounding-line meniscus is included in the analysis. In addition, surface tension is found to play a central role in the hysteresis observed during the initial stages of current propagation, determining whether the current remains confined or transitions to an unconfined state. Finally, we show that the self-similar solution is robust, remaining valid even when the inflow rate deviates from the ideal power-law form, for example, in cases involving a delay in filling the experimental cell.

Key words: gravity currents, non-Newtonian flows, lubrication theory

---

1. Introduction

Gravity currents are generated by density differences and appear when a fluid of density ρ advances into an ambient fluid of different density $\rho \pm \Delta\rho$ and the flow is primarily horizontal (Simpson 1997). Ungarish (2020) proposed a multifactor classification which makes it clear that several aspects of gravity-current dynamics remain insufficiently explored and warrant further investigation.

Among the outstanding issues, two are particularly relevant owing to their importance in industrial and environmental fluid mechanics: the influence of confinement and the role of surface tension effects. A central challenge lies in understanding how these two mechanisms interact, particularly in viscous gravity currents advancing under vertical confinement.

The significance of confinement was first established in the pioneering work of Nordbotten & Celia (2006) on CO_2 injection into porous formations, after which successive studies refined this framework or introduced alternative conceptual models for natural porous-media applications (Gunn & Woods 2011; Dudfield & Woods 2014; Farcas & Woods 2015; Guo *et al.* 2016; Pegler *et al.* 2017). Vertical confinement is also crucial for free-fluid viscous gravity currents in industrial settings, such as injection moulding (Hoffman 2014), thin-film coating and nasal drug delivery (Yang & Kowal 2025), as well as in environmental contexts (Taghavi *et al.* 2009; Zheng, Rongy & Stone 2015). A comprehensive synthesis of confinement effects is provided in the review by Zheng & Stone (2022).

Among the industrial configurations where confinement and capillarity potentially interact, the study of Hoffman (2014) is particularly instructive. By numerically simulating mould-filling in thin geometries, the author showed that gravity can noticeably modify the advance of viscous fluids in narrow gaps, influencing how reliably the cavity is filled. This motivates considering simplified idealised settings in which a viscous fluid is injected into a thin horizontal gap of height H representative of a long, shallow channel or a radially spreading layer. In such flows, the injected fluid may occupy the full gap over part of its extent while also forming a gravity-driven layer that spreads along the lower boundary, producing a coupled 'slug–gravity-current' structure. The relative development of these regions depends on the injection conditions, the gap height and the interplay between different forces.

Hutchinson, Gusinow & Worster (2023) extended these ideas by examining the confined axisymmetric propagation of a Newtonian fluid through a combined theoretical and experimental study. Using lubrication theory, they showed that a constant injection rate leads to a self-similar spreading behaviour in which the dynamics depends on a single dimensionless parameter characterising the ratio between the gap height and the characteristic height of the corresponding unconfined gravity current. Experiments using golden syrup injected into an air-filled gap of roughly one centimetre confirmed the theoretical predictions, with some deviations.

Building on this work, Hutchinson (2024) revisited the same axisymmetric configuration and showed that the observed discrepancies between theory and experiment can largely be attributed to the surface-tension effects at the grounding line. Although a complete Young–Laplace description predicts the formation of a meniscus whose height scales with the capillary length, the detailed shape and boundary conditions are sufficiently complex that a practical, fully resolved solution is not achievable. Instead, Hutchinson (2024) introduced a simplified representation in which the meniscus is modelled as an effective vertical jump of the order of a fraction of the height of the gap. This modification allows surface tension to be incorporated straightforwardly into the lubrication framework. A key outcome is that the underlying similarity structure of the surface-tension-free model is preserved, while the quantitative relationships between the governing dimensionless groups are shifted in a manner consistent with experiments. Although the effective height of the meniscus cannot be precisely prescribed, the study showed that estimates based on the ratio between the capillary length and the height of the gap offer a reasonable approximation. This extended model was developed and validated for Newtonian fluids in axisymmetric geometry.

Additional insight into the influence of surface tension comes from Zheng, Christov & Stone (2014), who reported that capillary forces may alter the far-field behaviour of convergent gravity currents to the extent that classical self-similar solutions no longer apply beyond a certain distance from the corner.

A further development is the extension to non-Newtonian rheology and multiple geometries. Ungarish (2025*b*) generalised the confined-flow theory to both two-dimensional and axisymmetric configurations, and to power-law fluids with rheological index n, recovering the Newtonian limit when $n = 1$. Within the lubrication framework, the author showed that self-similar spreading persists for specific injection laws determined by n, with distinct spreading exponents in the two geometries. As in the Newtonian case, the detached portion of the current develops a sloping interface whose shape must be obtained from an ordinary differential equation with conditions at the nose and grounding line. When surface tension is neglected, the scaled solution depends on a single confinement parameter and the theory provides a clear prediction of the threshold below which the current behaves as effectively unconfined, advancing along the lower boundary without contacting the upper one.

The present study builds on previous research in two complementary directions. First, it develops analytical solutions for vertically confined gravity currents of power-law fluids between parallel plates and with time-dependent injected volume, incorporating surface-tension effects at the grounding line, modelled as a vertical discontinuity of size σH following the approach of Hutchinson (2024), where $\sigma = \mathcal{O}(S)$ and $S = l/H \equiv (\Gamma/\rho g')^{1/2}/H$, with Γ the surface tension, l the capillary length, $g' = (\Delta\rho/\rho)g$ the reduced gravity and H the distance between the parallel plates. In doing so, it refines the framework of Ungarish (2025*b*) by explicitly accounting for surface tension and extends the methodology of Hutchinson (2024) to non-Newtonian fluids. Second, and constituting the main contribution, it provides experimental insight into the flow and assesses the accuracy of the theoretical predictions through a series of controlled tests with non-Newtonian fluids, including comprehensive rheological characterisation, thereby generalising the experimental methodology of Hutchinson *et al.* (2023) to non-Newtonian fluids.

An additional experimentally driven objective concerns the early-time behaviour of the gravity current, during which the similarity solution is expected to be inapplicable (Barenblatt 1996). Our results indicate that surface tension plays a key role in the hysteresis observed during these initial stages, controlling the transition between confined and unconfined flow regimes. The experiments were particularly challenging, requiring the simultaneous determination of the positions of the two fronts as well as precise measurements of the rheometric parameters and surface tension.

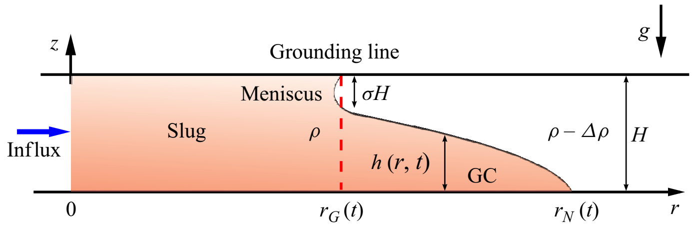

Figure 1. Sketch of the confined system: lubrication model for the GC with inclined interface. The height of the meniscus at the grounding line is σH. The volume (per radian) is $\mathcal{V} = qt^{\alpha}$. In the self-similar flow, $r_G = y_G K t^{\beta}$, $r_N = K t^{\beta}$ and r_G depends on the parameters J and σ. α, β, K, y_G are positive constants.

It should be noted that surface tension is also expected to generate a meniscus at the nose of the current, corresponding to a modification of the tip of the gravity current at the lower boundary, $r_N(t)$ in figure 1. This effect could, in principle, be incorporated into the similarity solution through an additional small parameter, σ_N. However, there is theoretical evidence (as specified later) that the influence of the nose meniscus is generally much smaller than that of the grounding-line meniscus; accordingly, in this study, we deliberately neglect its presence in the main analysis and discussion.

The manuscript is organised as follows. Section 2 presents the mathematical model and discusses the influence of surface tension in both two-dimensional and axisymmetric configurations. Section 3 describes the experimental set-up and analyses the corresponding results. Section 4 focuses on surface-tension-induced hysteresis phenomena, highlighting their dependence on the geometry of the experimental apparatus and on the test protocol. Section 5 provides a summary of the main findings and concluding remarks. Finally, the Appendix presents the assessment of the relevant shear-rate interval, carried out separately for the free-surface and confined regions of the gravity current (GC).

2. Theory

2.1. *Mathematical model*

The system of the gravity current (GC) is as sketched in figure 1. A three-dimensional (3-D) axisymmetric viscous GC of density ρ propagates within the confined gap between two horizontal parallel plates separated by distance H, displacing an ambient fluid with density $\rho - \Delta\rho$. The radii of the grounding line and the nose are $r_G(t)$ and $r_N(t)$, respectively. The formulation for viscous power law GCs without surface tension ($\varGamma = 0 \rightarrow \sigma = 0$) is presented by Ungarish (2025*b*). Here, we briefly summarise the extension for the system affected by the surface tension.

The mathematical model is based on several key simplifying assumptions: (i) the flow is axisymmetric-divergent from the origin in the cylindrical system, i.e. depending on the r, z coordinates (with no lateral velocity component); (ii) the flow of the ambient fluid is neglected, which is justified when the density and viscosity of the displaced fluid are significantly smaller than those of the GC. The interface between the fluids is expected to be stable with respect to the Taylor– Saffman effect and the reduced pressure, p, in the ambient fluid is constant (for definiteness, set to 0); (iii) the GC in the domain $r_G(t) < r \leq r_N(t)$ is a thin viscous layer of height $h(r, t) < H$, which admits the approximation of the lubrication theory (see, e.g. Ungarish 2020); (iv) at the grounding line $r = r_G(t)$, the interface of the GC is attached to the top by a vertical jump of height σH, which represents a surface tension meniscus. The real shape of the meniscus is readily identified in some snapshots of the experiments presented later.

We assume that $\sigma \leqslant 0.5$ (roughly, the capillary length is smaller than $0.5H$), in which case, the surface tension may be significant, but is not the dominant effect (as shown later). When surface tension is negligible, $\sigma = 0$. The real meniscus has a curved interface (determined by the solution of the Young–Laplace equation as mentioned previously, and as experimentally observed in some snapshots presented in the following). The typical radial extent of the meniscus is of the order of $H \ll r_N$ and, hence, the representation of the meniscus by a vertical jump is a consistent thin-layer approximation (we recall that the possible meniscus at the nose is presently ignored; this effect will be considered later in § 2.3).

In summary, a more detailed treatment of the moving contact-line dynamics at r_G and r_N is omitted, an assumption that is appropriate for the viscous–gravity-dominated regime characteristic of the present configuration.

The analysis can be performed in a convenient compact form for both Newtonian and non-Newtonian (power-law) fluids. We use dimensional variables unless stated otherwise.

The dynamic viscosity of the current is given by

$$\mu = m \left| \frac{\partial u}{\partial z} \right|^{n-1}, \tag{2.1}$$

where m is the consistency index and n is the fluid behaviour index (or exponent). We can also define $\nu = m/\rho$ of dimensions $[\mathrm{L}^2\mathrm{T}^{n-2}]$. A fluid is shear-thinning (pseudoplastic) if $n < 1$, shear-thickening (dilatant) if $n > 1$ and Newtonian if $n = 1$ (in this case, $m = \mu$, the standard dynamic viscosity of the fluid and ν is the standard kinematic viscosity coefficient). In the one-dimensional approximation adopted, the shear stress is given by $\tau_{zr} \equiv \tau = \mu(\dot{\gamma})\dot{\gamma} = m|\partial u/\partial z|^{n-1}\partial u/\partial z$, where $\dot{\gamma}$ is the shear rate. The power-law model was chosen over more sophisticated rheological models, such as the Ellis and Carreau–Yasuda models, for pragmatic reasons. The aim was to limit the number of rheological parameters and the overall complexity of the analysis while still capturing the essential non-Newtonian behaviour of the fluids. It is important to note that the power-law model, particularly for shear-thinning fluids, can perform poorly at low shear-rates, where it predicts an apparent viscosity that diverges; see, e.g. Longo *et al.* (2013*a*), Picchi *et al.* (2021), Boyko & Stone (2021). In the present framework, the power-law approximation is appropriate when the combination of propagation distance, inflow rate–time exponent and gap height ensures that the shear rates remain within the range over which the rheological behaviour is well described by a power-law based on rheometric measurements. The lowest shear-rate values are expected near the nose; the slower the nose during injection, the lower the shear rates and the greater the potential for reduced accuracy. Details on the assessment of the relevant shear-rate interval, distinguishing between the free-surface and confined regions of the gravity current, are provided in the Appendix.

The GC propagates in the r direction with velocity $u(r, z, t)$ and let $z = h(r, t)$ be the height of the interface above the bottom. The pressure in the thin-layer GC is hydrostatic, $p = g\Delta\rho(h - z)$, where g is the gravity acceleration. Therefore, the intrinsic driving force is given by $-g\prime(\partial h/\partial r)$, called the buoyancy. The effects of surface tension on the driving force are negligible because the interface is much larger than the σH meniscus. The buoyancy driving force is balanced by the shear, as expressed by the following lubrication-simplification momentum equation:

$$g\prime \frac{\partial h}{\partial r} - \nu \frac{\partial}{\partial z}\left[\left| \frac{\partial u}{\partial z} \right|^{n-1} \frac{\partial u}{\partial z} \right] = 0. \tag{2.2}$$

This equation is integrated twice with respect to z to obtain $u(r, z, t)$. The integration constants are determined by the boundary condition: (i) no slip $u = 0$ at the bottom $z = 0$ and (ii) no shear, $(\partial u/\partial z) = 0$, at the free interface $z = h$, $\quad r_G < r < r_N$. We obtain

$$u(r, z, t) = \frac{n}{n+1}\mathcal{G}^{1/n}\left(-\frac{\partial h}{\partial r}\right)^{1/n} h^{(n+1)/n}\left[1-\left(1-\frac{z}{h}\right)^{(n+1)/n}\right], \tag{2.3}$$

where

$$\mathcal{G} = g\prime/\nu. \tag{2.4}$$

The depth-averaged velocity is

$$\bar{u}(r, t) = \frac{1}{h}\int_0^h u(r, z, t)\,\mathrm{d}z = \frac{n}{2n+1}\mathcal{G}^{1/n}\left(-\frac{\partial h}{\partial r}\right)^{1/n} h^{(n+1)/n}. \tag{2.5}$$

The continuity equation is

$$\frac{\partial h}{\partial t} + \frac{1}{r}\frac{\partial}{\partial r}(hr\bar{u}) = 0. \tag{2.6}$$

In the following, we drop the upper bar in $\bar{u}$ and, unless stated otherwise, we refer to u as the depth-averaged velocity. The continuity equation and (2.5) form a set of equations for $u(r, t)$ and $h(r, t)$. The boundary conditions at the nose r_N are $h_N = 0$ while $u_N = \mathrm{d}r_N/\mathrm{d}t$. These conditions are not affected by the meniscus at the grounding line.

As noted by Hutchinson *et al.* (2023), Hutchinson (2024) and Ungarish (2025*b*), the effect of the confining boundary enters the mathematical model of the GC as a flux condition, rhu, at the moving grounding line. The presence of the meniscus affects this condition because $h = (1-\sigma)H$ at $r_G^+(t)$. The necessary flux condition is derived as follows.

Conservation of the total volume (per radian) is

$$\mathcal{V} = \frac{1}{2}r_G^2 H + \int_{r_G^+(t)}^{r_N(t)} h(r, t) r\,\mathrm{d}r = qt^\alpha, \tag{2.7}$$

where q is a positive coefficient, which describes the inflow rate (per radian) through the relation $\dot{V} = \alpha q t^{\alpha-1}$. We apply t derivative to (2.7) and use (2.6) to eliminate $\partial h/\partial t$. Recalling $h_N = 0$ and $h_G^+ = (1-\sigma)H$, we obtain the flux condition at r_G^+,

$$\sigma r_G \frac{\mathrm{d}r_G}{\mathrm{d}t} H + (rhu)_G = \alpha q t^{\alpha-1}. \tag{2.8}$$

2.1.1. *Dimensionless formulation*

We switch to dimensionless variables. The lengths are scaled with H and the volume (per radian) with H^3. The scales for velocity, time and flux coefficient are as follows:

$$U = \frac{n}{2n+1}\mathcal{G}^{1/n} H^{(n+1)/n}, \quad T = \frac{H}{U}, \quad Q_{scale} = \frac{H^3}{T^\alpha} \equiv H^{(3n+\alpha)/n}\left(\frac{n}{2n+1}\right)^\alpha \mathcal{G}^{\alpha/n}. \tag{2.9}$$

Subsequently, in this section, unless otherwise stated, the variables r, t, h, u, $\mathcal{V}$ and q are dimensionless, scaled as defined previously. The dimensional counterpart, when needed, will be denoted by an asterisk; in particular, we note that the dimensional flux coefficient, which will appear in the definition of J, is denoted q^*. The insight from the previous solution with no surface tension ($\sigma = 0$) suggests that the convenient parameter for expressing the importance of flow confinement is the dimensionless flux coefficient q

at some power. We note the scaling $Q_{scale} \propto H^{(3n+\alpha)/n}$ and this suggests the use of the following parameter:

$$J = q^{n/(3n+\alpha)} \equiv \left[\left(\frac{2n+1}{n}\right)^{\alpha} q^* \mathcal{G}^{-\alpha/n}\right]^{n/(3n+\alpha)} \frac{1}{H} = \frac{L}{H}. \tag{2.10}$$

The right-hand side of (2.10) is the ratio of a length, L, to H. This expresses the ratio of the typical thickness of the unconfined GC to H.

2.2. *The similarity solution*

The dimensionless depth-averaged velocity is

$$u(r,t) = \left(-\frac{\partial h}{\partial r}\right)^{1/n} h^{(n+1)/n}. \tag{2.11}$$

We substitute (2.11) into the continuity equation (2.6) and introduce the reduced horizontal coordinate of the GC,

$$y = r/r_N(t), \tag{2.12}$$

where $0 < y \leq 1$. The governing equation of the GC, in terms of y and t, reads as follows:

$$\frac{\partial h}{\partial t} - y\frac{\dot{r}_N}{r_N}\frac{\partial h}{\partial y} + \frac{1}{r_N^{(n+1)/n}}\frac{1}{y}\frac{\partial}{\partial y}\left[y h^{(2n+1)/n}\left(-\frac{\partial h}{\partial y}\right)^{1/n}\right] = 0, \tag{2.13}$$

where the upper dot denotes the time derivative. The nose of the GC is at $y = 1$, where the boundary condition is

$$h = 0 \quad \text{for} \quad y = 1, \tag{2.14}$$

and the grounding line is at y_G, where the following boundary condition holds:

$$h = 1 - \sigma \quad \text{for} \quad y = y_G. \tag{2.15}$$

The solution of (2.13) is of interest in the domain $y_G \leq y \leq 1$. We argue that the cases of interest must have a constant $y_G \in (0, 1)$; otherwise, y_G will migrate to either 0 (unconfined GC) or 1 (full slug). Such a non-trivial system appears when both r_G and r_N propagate like t^β, where β is a constant.

We therefore attempt a similarity solution of the form

$$r_N(t) = K t^\beta, \quad r_G(t) = y_G K t^\beta, \tag{2.16a}$$

$$h(y,t) = h(y) = K^{(n+1)/(n+2)}\lambda(y), \quad u(y,t) = [\lambda^{n+1}(-\lambda')]^{1/n} K t^{\beta-1}, \tag{2.16b}$$

where the prime denotes derivative with respect to y. The choice $h = h(y)$ means that the current elongates with time, but maintains the thickness at the points $y = r/r_N$. This special form of h follows from the observation that h must be constant, $1 - \sigma$, at the grounding-line position $y = y_G$. The variable $\lambda(y)$ represents the thickness (height) of the GC. The scaling of this variable renders some benefits which will be seen later.

The existence of the similarity solution is not guaranteed *a priori*. We must demonstrate that the postulated flow satisfies the equations and boundary conditions with physical values of β and K.

For a given n, the substitution of the similarity behaviour (2.16) into the continuity equation (2.13) imposes the condition

$$\alpha = \frac{2n}{n+1}, \quad \beta = \frac{\alpha}{2} \equiv \frac{n}{n+1}, \tag{2.17}$$

and yields the equation

$$\left[y\lambda^{(2n+1)/n}\left(-\lambda'\right)^{1/n}\right]' - \beta y^2\lambda' = 0, \tag{2.18}$$

where the prime symbol indicates derivation. The nose condition $\lambda(1) = 0$ (i.e. $h_N = 0$) justifies the Frobenius-series result

$$\lambda(y) = \left[(n+2)\beta^n(1-y)\right]^{1/(n+2)} \equiv \left[(n+2)\left(\frac{n}{n+1}\right)^n(1-y)\right]^{1/(n+2)} \quad (y \to 1). \tag{2.19}$$

This provides values of λ and λ' at $y = 1 - \varDelta$, for a small $\varDelta$, which allow numerical integration of (2.18) to smaller y. We conclude that the height profile $\lambda(y)$ of the interface of the GC for $y \in (y_0, 1)$ can be obtained by a standard numerical method (we used fourth-order Runge–Kutta; y_0 is a small number which mimics the finite radius of the source, we used 0.05). This $\lambda(y)$ we call 'general (or universal) profile' because it does not depend on J and σ (only on n). Actually, this is the profile of an unconfined GC with influx power α given by (2.17).

Next, we consider the flux boundary condition (2.8). We find that this condition, applied at a fixed y_G, is compatible with the similarity assumption (2.16) when $\beta = \alpha/2$ (independent of the value of σ).

The calculation of J and K can now be performed for a given pair of y_G and σ. At position $y = y_G$, where λ_G and λ'_G are known (from the general profile), we apply the grounding-line condition (2.15) and volume flux (2.8). After some algebra, this yields the following:

$$K = \left[(1-\sigma)/\lambda_G\right]^{(n+2)/(n+1)}, \tag{2.20}$$

$$q = J^{3+\alpha/n} \equiv (K^2 y_G/\alpha)\left[(1-\sigma)(-\lambda'_G\lambda_G^{n+1})^{1/n} + \beta\sigma y_G\right]. \tag{2.21}$$

For given n, σ and y_G, we obtain the values of J and K of the confined GC. For $\sigma = 0$, we recover the results of Ungarish (2025*b*). Physically acceptable results were obtained for all tests in the plausible parameter range of n, σ and $y_G \in (0.05, 0.99)$. This confirms the validity of the similarity solution. The point $y_G = 0.05$, where $J = J_0$, is considered the onset of the confinement effect; GCs with $J < J_0$ are considered free (unconfined) and outside the scope of the present work. The results of Hutchinson *et al.* (2023) and Hutchinson (2024) are recovered for $n = 1$ (but note that these papers use a different scaling of the variables).

It is remarkable that the presence of the meniscus $\sigma > 0$ has little effect on the theoretical flow pattern. The similarity behaviour of the grounding line and nose position, $\sim t^\beta$, for select values of α, are the same as for $\sigma = 0$. The variables K, J and y_G depend on σ. In the domain $r_G(t) < r \le r_N(t)$, the height profile $\lambda(y)$ of the interface of the GC is also unaffected and actually the same as for an unconfined GC.

We emphasise that the similarity solution for the confined GC exists only for the select values of α given by (2.17). The corresponding influx is able to sustain the grounding line height $h = 1 - \sigma$ at a fixed y_G. For a smaller (or larger) α, the grounding line y_G will migrate to 0 (or 1).

2.3. *Nose meniscus*

To complete the formulation, we show that a nose meniscus can be implemented in the similarity solution as follows. The meniscus is modelled as a vertical front of height (dimensionless) σ_N. The relevant conditions at $y = 1$ are $h_N = \sigma_N > 0$ and $u_N =$

$\mathrm{d}r_N/\mathrm{d}t = \beta K t^{\beta-1}$. The differential equation for $\lambda(y)$ and the flux condition at the grounding line are not affected (the derivation of (2.8) is slightly modified because $h_N > 0$). When $\sigma_N > 0$, modification of the formulation is needed for the condition for λ at the nose. These are (see 2.16*b*)

$$h_N = K^{(n+1)/(n+2)}\lambda(1) = \sigma_N, \tag{2.22}$$

$$\lambda'(1) = -\beta^n \lambda(1)^{-(n+1)}. \tag{2.23}$$

Equation (2.23) expresses the condition $u_N = \beta K t^{\beta-1}$. Calculating the similarity scaled height-profile $\lambda(y)$ is now implicit, because the unknown K appears in the boundary conditions at $y = 1$ and y_G, see (2.22) and (2.20). Therefore, $\lambda(y)$ is no longer a universal profile (dependent only on n) as before. For each combination of parameters, an iteration is needed, such as: for a fixed y_G and given n, σ, σ_N, guess an initial K, use (2.22)–(2.23) to integrate (2.18) for $\lambda(y)$ from $y = 1$ to y_G, calculate the new K by (2.20) and repeat the solution with a corrected K until convergence of K is achieved. Moreover, we note that the values of $\alpha(n)$ imposed by (2.17) for the confined flow are below the critical $\alpha_c(n) = 2(n + 5)/(n + 3)$ (see Ungarish 2020, § 14.3.2). This validates the use of the viscous lubrication framework for long periods of propagation. Then, calculate J by (2.21).

This iteration complicates the solution. However, various numerical tests performed by Hutchinson (2024) and in the present work (not shown) indicate that the influence of surface tension on K and y_G is dominated by the meniscus at the grounding line, i.e. the value of σ; the increase of σ_N from 0 up to σ turns out to be a small perturbation. These lubrication-theory conclusions are supported by box-model results (Ungarish 2025*a*). In other words, the formulation of § 2.2 with $\sigma_N = 0$ is sufficient for the prediction of the surface tension effects in the similarity flow under investigation. It is remarkable that the presence of the menisci $\sigma > 0$ and $\sigma_N > 0$ has little effect on the theoretical flow pattern. The similarity behaviour of the grounding line and nose position, $\sim t^\beta$, for select values of α, are the same as for the system without surface tension, whereas the variables K, J and y_G are affected by the menisci.

2.4. *Summary and discussion of similarity solution results*

A given n determines the influx rate α and the propagation rate β. Next, the model has two input parameters that depend on the gap H: J and σ. These parameters determine the position of the grounding line, y_G, and the propagation coefficient, K. The dependencies between y_G, J, K and σ must be determined numerically through the solution $\lambda(y)$.

The careful reader may ask: why restrict the analysis to similarity solutions that cover a somewhat restricted domain of α? The answer is that the similarity behaviour is essential in the present problem, because it keeps the grounding line between the source and the nose for a significant period/distance of propagation. Influx with a different α is bound to produce a very different flow pattern. For the selected α, the GC elongates, but maintains a constant average thickness. When α is reduced, the GC tends to become thinner with t, the grounding line moves towards the inlet and an unconfined GC appears at the bottom of the gap. When α increases, the GC tends to thicken with t, the grounding line moves towards the nose and the injected fluid behaves like a slug in contact with both boundaries of the gap. It is remarkable that the similarity solution is robust: for a given geometry, the time powers α and β depend on n, and are unaffected by the presence of surface tension effects represented by σ and σ_N.

For generic values of α, it is always possible to find a numerical solution in the space–time domain and this generalises the approach for application purposes. However, it fails to capture the equilibrium among β_G, β_N, n and α when the relationships among these parameters satisfy the self-similarity condition. For this reason, the model of the effects of surface tension, which is designed to preserve the self-similarity solution, is even more valuable, as it enables the use of a powerful tool that can be applied to a wide range of flows, with stringent analytical and experimental validations.

2.5. *Implementation to present experiments*

For each experiment, the value of the parameters of the fluid n, m, ρ and Γ are measured, and this determines the value of α of the corresponding pump setting and the value of ν. Here, $g' = g$ because the ambient fluid was air, and the gap H and the influx parameter q^* are set in the experiment. We obtain the value of J by (2.10).

We recall that the accurate value of the surface tension parameter σ is not available for practical systems. Comparisons of predictions with data performed by Hutchinson (2024) suggest that $\sigma \sim S = l/H$, where S is the capillary number and $l = (\Gamma/\rho g')^{1/2}$. This is a good starting point for the practical use of the present models (however, we must keep in mind that the data set of Hutchinson *et al.* (2023) covers only the flow of a Newtonian fluid) and we treated σ as an adjustable constant. For each experiment (that is, given n and J), we run the model with various values of σ in a range similar to theoretical suggestion of the capillary number S. By comparing the simulated results y_G and K with the appropriate measured values, we chose the optimal σ, as shown in table 1.

3. Experiments

3.1. *Experimental set-up and protocol*

We performed a series of experiments in which different types of fluid were injected between two plates of polymethylmethacrylate (PMMA) through a circular hole in the centre of the lower plate. Fluids were injected through a circular hole with a diameter of 25 mm connected to a syringe pump that contained a maximum of 500 ml of fluid. The tests were performed with four shear-thinning fluids, a Newtonian fluid and a shear-thickening fluid. The latter fluid displayed two distinct sets of rheometric parameters, arising from the different temperatures at which the tests were conducted. Four different gap sizes were used, ranging from 5.5 to 12.7 mm, although for the latter space, the GCs were always unconfined. The gap spacings, controlled by calibrated lock nuts, were 5.5 ± 0.3 mm, 7.8 ± 0.3 mm, 9.3 ± 0.3 mm, 12.7 ± 0.3 mm. The plates are square, with 45 cm side length and 1 cm thickness, and are spaced apart with calibrated metal nuts. Using a quick and conservative calculation method, with a Young modulus $E = 30$ GPa and a specific weight of 12 000 N m^{-3}, we estimate that the maximum vertical deflection of the upper plate due to weight is approximately 25 µm. The internal pressure required to drive the gravity current acts in opposition to the weight of the upper plate, i.e. it counteracts this weight, while the lower plate, supported rigidly on three adjustment wheels, is assumed to remain undeformed. Assuming an average overpressure of 100 Pa, the average (negative) vertical deflection is almost equal to the average (positive) vertical deflection induced by the weight of the plate.

The syringe pump was made with a piston moved by a slide on a recirculating ball screw, with a DC motor with gear reducer controlled in feedback with position measured by a linear potentiometer. Two different motor reduction ratios were used to ensure greater torque for the shear-thickening fluid, which is characterised by higher apparent viscosity. The maximum flow rate is 40 cm^3 s^{-1}, controlled with an overall accuracy of 0.5 %. A schematic of the experimental set-up is shown in figure 2.

https://doi.org/10.1017/jfm.2026.11677 Published online by Cambridge University Press

Test	n	m (Pa s^n)	ρ (kg m^{-3})	l (mm)	q^* (ml s$^{-\alpha}$)	H (mm)	J	α_{th}	α_{exp}	β_{th}	$\beta_{G\text{-}exp}$	$\beta_{N\text{-}exp}$	S	σ	$y_{G\text{-}th}$	G_{exp} (mm s$^{-\beta_G}$)	N_{exp} (mm s$^{-\beta_N}$)	$y_{G\text{-}exp}$	K_{th}	K_{exp}
1	0.29	1.45	1000.2	2.60	7.87	5.5	0.80	0.455	0.46	0.227	0.22	0.22	0.47	0.40	0.783	54.34	56.43	0.96	0.961	0.97
2	0.29	1.45	1000.2	2.60	7.87	7.8	0.56	0.455	0.46	0.227	0.23	0.23	0.33	0.40	0.559	43.93	49.40	0.89	0.507	0.43
3	0.29	1.45	1000.2	2.60	7.91	9.3	0.47	0.455	0.46	0.227	0.22	0.22	0.28	0.40	0.469	33.11	56.92	0.58	0.381	0.41
4	0.29	1.45	1000.2	2.60	8.03	12.7	0.35	0.455	0.46	0.227	0.00	0.22	0.20				61.84			0.25
5	0.44	0.79	1046	2.01	6.33	5.5	0.73	0.615	0.62	0.308	0.31	0.31	0.37	0.50	0.829	47.90	47.94	1.00	0.803	0.69
6	0.44	0.79	1046	2.01	6.38	7.8	0.52	0.615	0.61	0.308	0.32	0.31	0.26	0.50	0.609	34.98	46.93	0.75	0.444	0.37
7	0.44	0.79	1046	2.01	6.37	9.3	0.43	0.615	0.62	0.308	0.33	0.31	0.22	0.45	0.334	17.24	53.75	0.32	0.346	0.33
8	0.44	0.79	1046	2.01	6.37	12.7	0.32	0.615	0.62	0.308	0.00	0.30	0.16		0.088		56.96		0.216	0.21
9	0.70	0.40	1213.9	1.76	5.92	5.5	0.69	0.827	0.85	0.413	0.41	0.41	0.32	0.50	0.825	49.02	49.67	0.99	0.731	0.76
10	0.70	0.40	1213.9	1.76	6.05	7.8	0.50	0.827	0.84	0.413	0.42	0.42	0.23	0.50	0.602	30.08	50.23	0.60	0.436	0.42
11	0.70	0.40	1213.9	1.76	6.22	9.3	0.42	0.827	0.83	0.413	0.40	0.40	0.19	0.50	0.432	12.30	56.10	0.22	0.342	0.40
12	0.70	0.40	1213.9	1.76	6.29	12.7	0.31	0.827	0.83	0.413	0.00	0.41	0.14	0.50	0.103		56.70		0.227	0.23
13	0.82	0.42	1225.7	1.56	3.94	5.5	0.72	0.903	0.91	0.452	0.43	0.43	0.28	0.45	0.817	41.79	42.55	0.98	0.799	0.90
14	0.82	0.42	1225.7	1.56	3.97	7.8	0.51	0.903	0.90	0.452	0.45	0.45	0.20	0.45	0.557	23.12	42.11	0.55	0.469	0.48
15	1.00	0.09	1204.0	1.90	2.42	5.5	0.49	1.000	1.00	0.500	0.00	0.50	0.35	0.20	0.145		30.70		0.487	0.35
16	1.00	0.09	1204.0	1.90	6.28	7.8	0.44	1.000	1.00	0.500	0.50	0.50	0.24	0.56	0.617	29.51	47.56	0.62	0.440	0.32
17	1.00	0.09	1204.0	1.90	6.55	9.3	0.37	1.000	1.00	0.500	0.50	0.50	0.20	0.50	0.334	13.88	51.91	0.27	0.305	0.27
18	1.28	1.45	1540.3	2.50	0.79	5.5	0.81	1.125	1.13	0.562	0.56	0.56	0.45	0.50	0.931	16.98	17.53	0.97	0.976	0.96
19	1.28	1.45	1540.3	2.50	0.79	7.8	0.57	1.125	1.13	0.562	0.56	0.56	0.32	0.40	0.647	5.03	17.42	0.29	0.581	0.58
20	1.41	1.05	1545.0	2.40	0.79	9.3	0.47	1.170	1.17	0.585	0.59	0.59	0.26	0.35	0.375	5.16	16.36	0.32	0.461	0.41
21	1.28	1.45	1540.3	2.50	0.80	12.7	0.35	1.125	1.13	0.562	0.00	0.57	0.20	0.30	0.000		16.73		0.320	0.27

Table 1. List of the experiments. Here, n is the fluid behaviour index; m is the consistency index; ρ is density; $l=\sqrt{\Gamma/(\rho g\prime)}$ is the capillary length, where Γ is the surface tension and $\rho g\prime$ is the reduced specific weight; q^* is the coefficient of the injected volume of fluid (per radian); α is the theoretical/experimental time exponent of the injected volume of fluid; $\beta_{G,N}$ are the time exponents of the grounding line and nose positions; S is the capillary number; σ is the parameter used to incorporate the meniscus effect, $y_G=r_G/r_N$ is the ratio of grounding line to nose positions (theory and experiments); G_{exp} and N_{exp} are the experimental dimensional coefficients for the grounding line and nose positions, respectively; and K is the dimensionless coefficient governing the temporal evolution of the nose position.

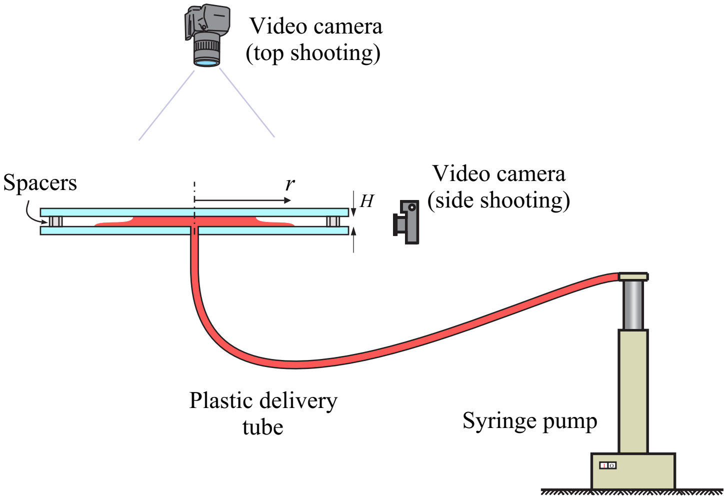

Figure 2. Schematic of the experimental set-up.

The shear-thinning fluids were obtained by mixing water, glycerol and Xanthan Gum in various proportions, adding biocide to prevent bacterial degradation, and food dye for easy visualisation. The shear-thickening fluid was a suspension of corn starch in a mixture of salt (K_2HPO_4) plus water (900 g in one litre of salt water), with a density of 1563 kg m^{-3} at a temperature of 18 °C to prevent sedimentation. This shear-thickening fluid is a new concept compared with traditional cornstarch in aqueous suspension, which is subject to sedimentation with separation of the two phases in a relatively short time. Furthermore, the high salt concentration inhibits biodegradation, without the need to add biocides. The density of the fluids, ranging from 1000 to 1540 kg m^{-3}, was measured with an Anton Paar DM5000 densimeter, with an accuracy of 0.01 %; the rheometric properties were measured with an Anton Paar MCR101 rheometer, with parallel plates of 25 mm in diameter. The measurement temperature was set equal to the room temperature, ensuring that no significant variations occurred during the experiments.

Figure 3 shows the experimental and theoretical curves $\tau(\dot{\gamma})$. The experimental curves (symbols) were obtained by rheometric measurements, while the theoretical curves represent the power-law relationship between shear stress and shear-rate for the different fluids used in the experiments. It can be seen that the power-law relationship is well satisfied within the range of shear rates present in the experiments. This range has been determined from the curves presented in figure 13 of the Appendix, with the fluid behaviour index obtained by interpolation within the anticipated shear rate interval.

The surface tension was measured with a force tensiometer based on a Du Noüy ring, a platinum iridium ring having a circumference of 60 mm, measuring the maximum traction force with a scale with an accuracy of 10^{-4} N.

The displaced fluid is air, whose density and dynamic viscosity are negligible compared with those of the injected fluid. In particular, its much lower viscosity relative to the apparent viscosity (or the effective viscosity for Newtonian tests) suppresses Saffman–Taylor instabilities, which were indeed not observed.

The two fronts, nose and grounding line, of the gravity current were measured from the top with a video camera at 25 frames per second and a resolution of 1920 × 1080 pixels. The geometric reference is provided by a radial grid superimposed on the current through video processing. For some of the experiments, a second video camera was placed in the

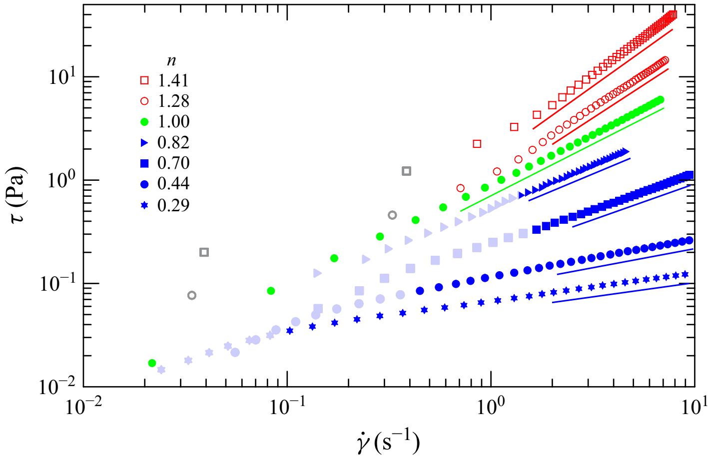

Figure 3. Results of rheometric measurements for the fluids used in the experiments. The shear rate $\dot{\gamma}$ is shown on the horizontal axis and the shear stress τ on the vertical axis. The experimental relationship $\tau(\dot{\gamma})$ is illustrated by symbols: red, green and blue symbols refer to shear-thickening, Newtonian and shear-thinning fluids, respectively. The datasets have been vertically shifted for ease of visualisation. The data scatter for low shear rates, especially for shear-thickening fluids, reflects the nature of these fluids, whose rheological behaviour follows a power-law form only above a threshold shear rate. The grey symbols correspond to shear rates below the minimum theoretical shear rate in each experiment, as reported in figure 13. The solid lines represent the theoretical relationship $\tau = m\dot{\gamma}^n \equiv \mu\dot{\gamma}$ (2.1), where the flow behaviour index n and the consistency index m are determined by excluding the grey data points from the analysis.

side view to record the GC profile in the radial direction. Figure 4 shows the side and top view of a confined GC of a shear-thinning fluid. To visualise the portion of the gravity current that advances with a free surface, i.e. without contact with the upper plate, side illumination was applied using a strip of LEDs aligned parallel to the cell gap.

The position of the two fronts, or of the single front (nose), in the case of unconfined GC, is the result of the quadratic mean of the position measured along four directions separated by 90° or eight directions separated by 45°, depending on the lesser or greater symmetry. In this regard, to ensure high symmetry of the GC, it was necessary to check the horizontality of both sheets with a spherical level and to clean the surfaces in contact with the fluid very thoroughly to prevent fluid residues and dirt of various origins from interfering with the advancement of the two fronts.

The Reynolds number is first defined in its classical form for gravity currents as $Re = (\rho\overline{u}L)/\mu$ (Mukherjee & Balasubramanian 2020), where $\overline{u}$ is the horizontal depth-averaged velocity of the current, L is a characteristic length scale and μ the fluid dynamic viscosity. This definition assumes a constant viscosity and is therefore appropriate for Newtonian fluids. For non-Newtonian power-law fluids, this formulation is extended by incorporating the rheological parameters directly, following Darby (1986) and Ng & Mei (1994). In this case, the Reynolds number is estimated as $Re = [\rho\overline{u}^{2-n}(H/2)^n]/m$, where $L = H/2$ is the hydraulic radius of the cylindrical cross-section, and m and n are the consistency and power-law indices, respectively. This provides a consistent generalisation of the classical definition to flows with shear-dependent viscosity. The corresponding critical Reynolds number is $Re_c = 0.125[(3n+1)/(2n)]^n[2100 + 875(1-n)]$.

For the maximum imposed flow rate and at a distance $r = r_0 = 1.25$ cm from the axis (where r_0 is the radius of the inlet pipe), the highest Reynolds number is $Re = 160 \pm 10\,\%$ for experiment 1 in table 1, corresponding to a shear-thinning fluid with $n = 0.29$, while

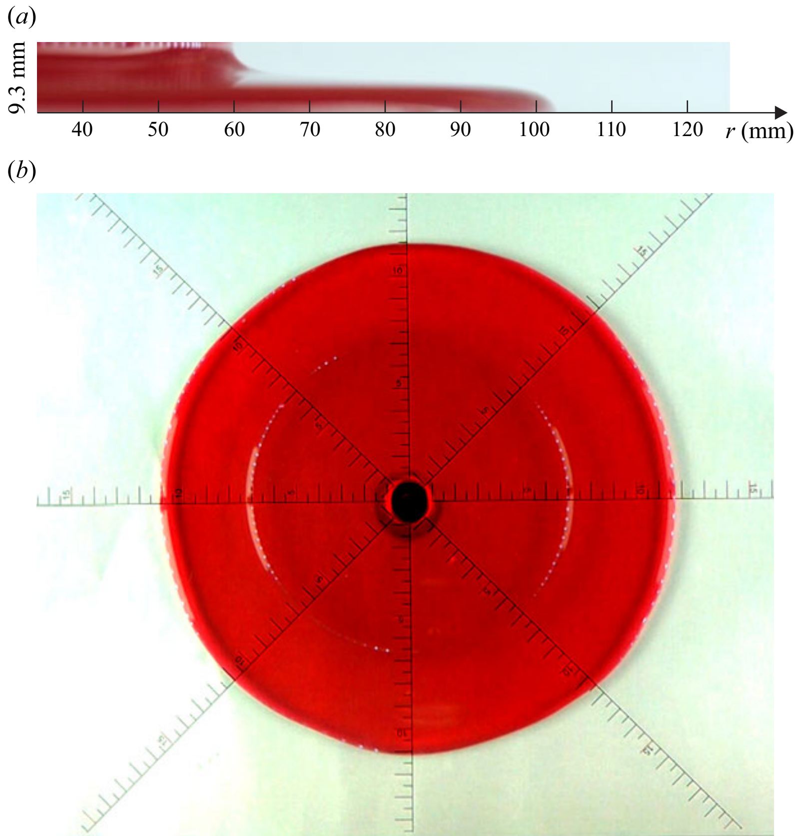

Figure 4. Snapshot at $t = 32$ s of a GC of shear-thinning fluid advancing in a gap with $H = 9.3$ mm, experiment 3. (*a*) Side view and (*b*) top view.

the corresponding nominal critical Reynolds number is $Re_c = 480 \pm 5\,\%$. For all other experiments, the maximum Reynolds number evaluated at the same radial location is lower than 160, whereas the critical Reynolds number is always greater than 480. Other estimates of Re for the GC, e.g. (8.30) of Ungarish (2020), support the present conclusions.

The uncertainty in the estimates of n and m is mainly due to the non-viscometric nature of the flow field reproduced in the rheometer and, to an even greater extent, to the approximation of the power-law model and to temperature variations during the tests. The combined effects lead to $\Delta n/n \leq 5\,\%$ and $\Delta m/m \leq 9\,\%$. The density of the fluid was measured with high accuracy, but is again subject to temperature fluctuations; hence, $\Delta\rho/\rho \leq 0.2\,\%$. The capillary length is estimated with uncertainty $\Delta l/l \leq 0.5\,\%$ and the influx coefficient has uncertainty $\Delta q^*/q^* \leq 0.5\,\%$. The width of the gap has uncertainty $\Delta H/H \leq 5\,\%$; for the parameter J, it results in $\Delta J/J \leq 11.5\,\%$. The uncertainties associated with β, G_{exp} and N_{exp} were estimated using a Monte Carlo simulation (see, e.g. Papadopoulos & Yeung 2001). All variables and parameters involved were assumed to follow Gaussian distributions, with mean values taken as their experimentally measured means and variances given by the squares of the corresponding relative experimental uncertainty. Random samples drawn from these distributions were combined through the theoretical model to obtain realisations of β, G and N; repeating the procedure yielded statistical samples from which mean and variance estimators were computed.

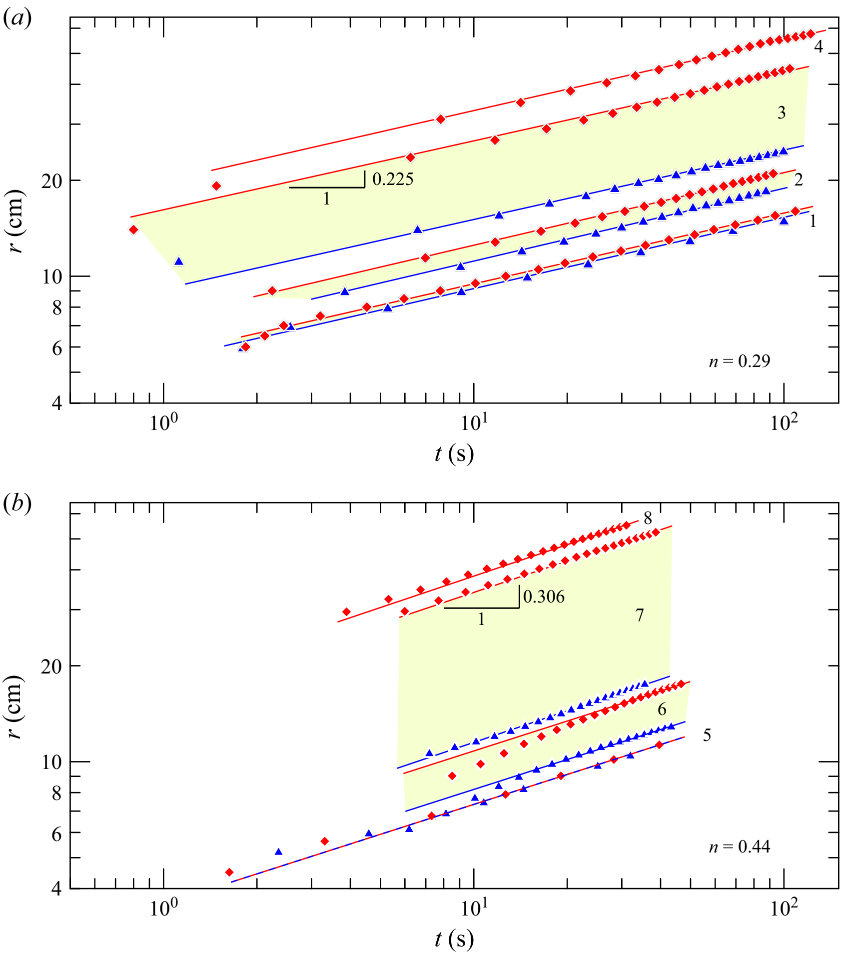

Figure 5. Time series of the front position for (*a*) experiments 1–4 for $n = 0.29$ and (*b*) experiments 5–8 for $n = 0.44$. The red and blue symbols denote the nose and grounding line, respectively. The straight lines show the theoretically predicted slopes. The shaded region connects the position of the nose and the ground within the same test, and is missing for tests with detached GC in which only the nose was observed. Some of the data points have been shifted vertically for clarity.

The simulation consisted of 10 000 runs, assuming uncertainties of 1/50 s in time measurements and 3 mm in the detection of the front position in time. The resulting relative uncertainties satisfy $\Delta\beta/\beta \leq 2.5\,\%$, $\Delta G_{exp}/G_{exp} \leq 2.5\,\%$, $\Delta N_{exp}/N_{exp} \leq 2.5\,\%$. Consequently, $\Delta r_G/r_G \leq 5\,\%$ and $\Delta K/K \leq 8.5\,\%$.

3.2. *Experimental results*

Table 1 shows the list of experiments, as well as the theoretical and experimental values of the most significant variables. We cover the ranges $0.29 \leq n \leq 1.43$, $0.46 \leq \alpha \leq 1.17$, $0.35 \leq J \leq 0.8$ and $0.20 \leq \sigma \leq 0.56$, with a capillary number $0.14 < S < 0.47$ (the previously published experiments of Hutchinson *et al.* (2023) cover $n = 1$, $\alpha = 1$, $0.36 \leq J \leq 1.24$, $0.16 \leq \sigma \leq 0.34$).

Figures 5, 6 and 7 show the time evolution of the positions of the two fronts for all the experiments with a different value of J. The lines are asymptotic mean curve fits.

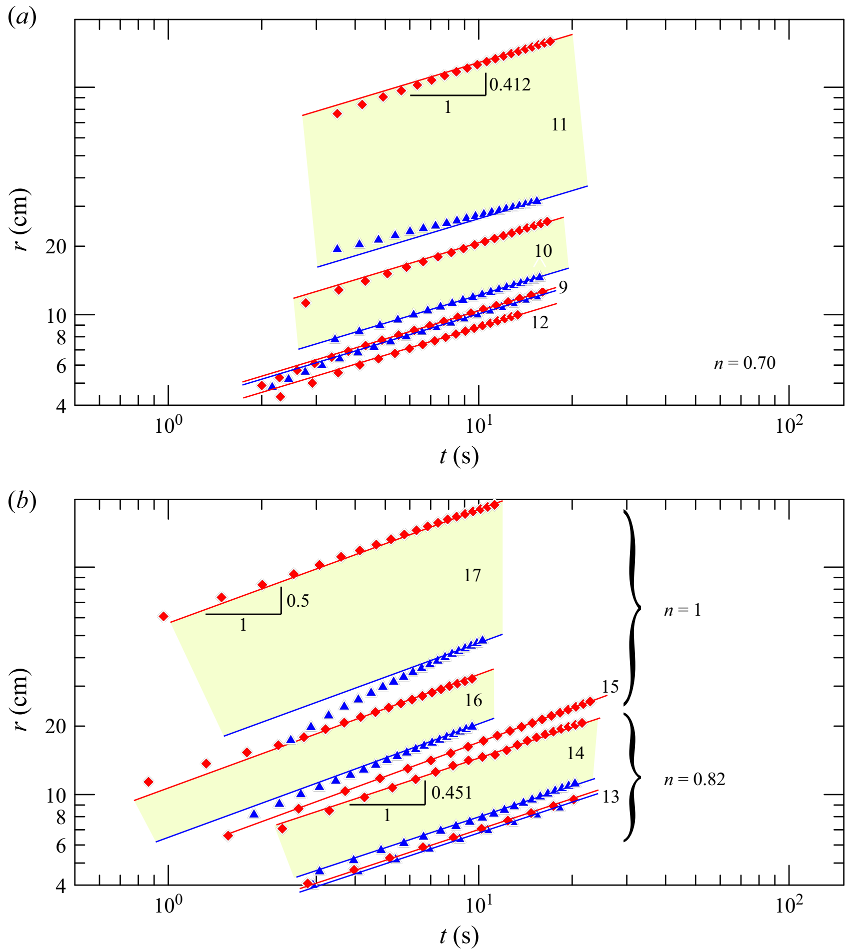

Figure 6. Time series of the front position for (a) experiments 9–12 for $n = 0.70$ and (b) experiments 13–17 for $n = 0.82$, 1. For caption, see figure 5.

As expected, except for early times, the position in time of the fronts is interpolated by power functions with the same values of the exponents β_G and β_N, and differs only in the coefficients G and N, as predicted by the theory. Of the two fronts, the grounding line appears to reach the asymptotic regime more slowly.

Figure 8 shows a comparison between theoretical and experimental values of K and y_G, with better agreement for the former parameter. A motivation for the different degree of approximation is provided by the diagrams showing K and y_G as a function of J in figures 4(c) and 5(c) of Ungarish (2025b). The curves associated with y_G are flatter than those of K, indicating that y_G is more sensitive: small variations in J lead to significant changes in y_G, whereas the corresponding changes in K are smaller, particularly for moderate values of J. In addition, the hysteresis phenomena – discussed in detail later – introduce variability in the dynamics of these GCs, with effects more pronounced in K than in y_G.

Figure 9 shows a comparison between the present experiments and those performed by Hutchinson *et al.* (2023), which were also interpreted by incorporating surface tension effects as described by Hutchinson (2024). Notably, even in those experiments, the agreement is stronger for K than for y_G. For the latter, therefore, the same degree of results scatter observed in our non-Newtonian fluid experiments is evident.

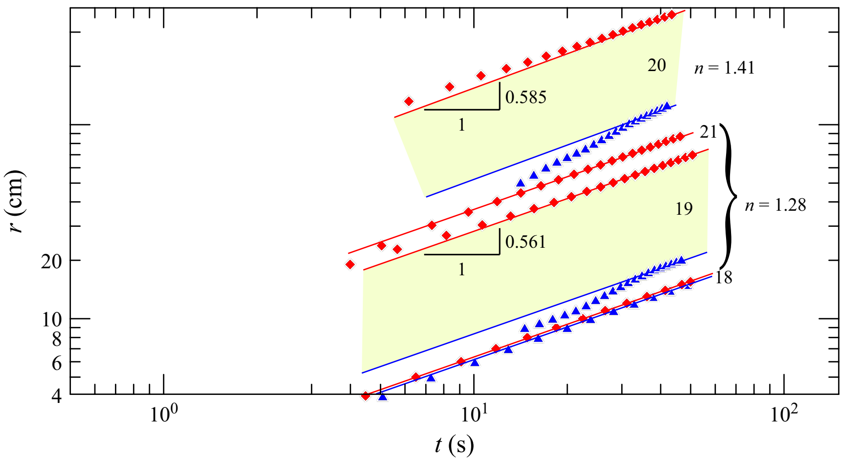

Figure 7. Time series of the front position for experiments 18–21 for $n = 1.28$, 1.41. For caption, see figure 5.

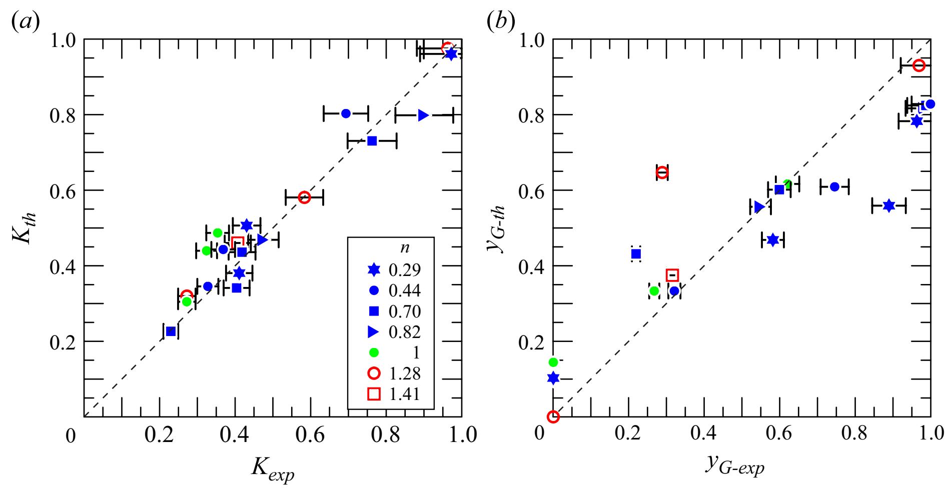

Figure 8. Comparison between theory and experiments (a) for the values of K and (b) for the values of y_G. The dashed lines indicate the perfect agreement.

4. Hysteresis due to surface tension

In this section, we describe phenomena observed during the early evolution of the gravity current, which we group under the general category of hysteresis effects. Here – consistent with common usage in the physical sciences – hysteresis denotes the dependence of a system's current state or response on its past history, rather than solely on its current conditions. In the present context, these effects are closely tied to the role of surface tension, which, although already incorporated into the governing equations admitting self-similar solutions, also exerts a significant influence during the initial stages of propagation. This influence is particularly pronounced near the axis where the fluid is introduced, where surface-tension-driven mechanisms affect the subsequent evolution of the current.

The literature documents that, even in flow fields that are, on the whole, ostensibly simple, hysteresis phenomena arise. These phenomena have been extensively investigated by the scientific community, with a particularly significant contribution by Kistler &

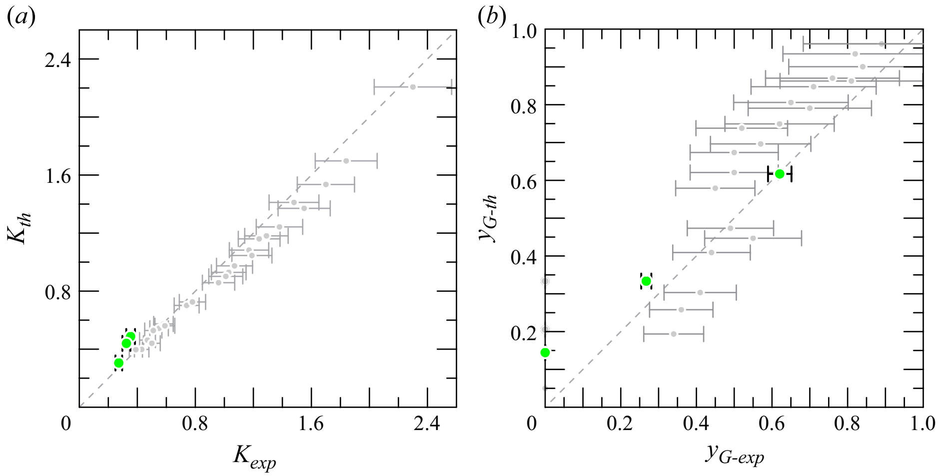

Figure 9. Comparison between theory and experiments for Newtonian fluids, the present tests (green symbols) and for the experiments by Hutchinson *et al.* (2023) (grey symbols) further analysed by Hutchinson (2024), (*a*) for the values of K, and (*b*) for the values of y_G. The dashed lines indicate the perfect agreement.

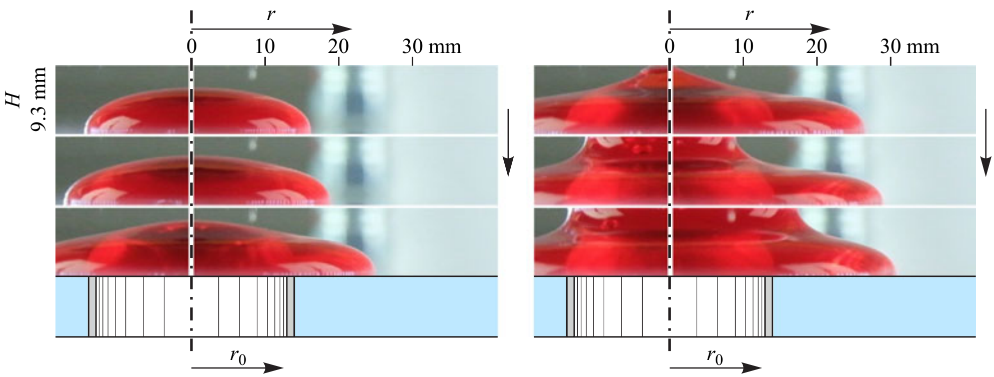

Figure 10. Time evolution (top to bottom and left to right) of GC in the initial phase for experiment 3, shear-thinning fluid with $J = 0.47$. The dome leading to the attachment of the current to the cell top plate can be observed. $r_0 = 1.25$ cm is the radius of the inlet pipe.

Scriven (1994), on the so-called 'teapot effect' which is, in turn, cited by Hutchinson *et al.* (2023) and Hutchinson (2024).

When examining the flow rate in relation to the fluid behaviour index, we observe a waning inflow for shear-thinning fluids, a waxing inflow for shear-thickening fluids and a steady inflow for Newtonian fluids. Moreover, the initial flow rate evidently tends to zero for $t \to 0$. This implies that for shear-thinning fluids, the inflow rate exhibits an initial increase and reaches a maximum, followed by a decline. If the flow adheres to the upper boundary of the cell at the maximum inlet flow rate, it propagates with two distinct fronts, even when the corresponding value of J predicts a detached gravity current. Figure 10 shows the initial evolution of the GC profile for experiment 3, with a dome that causes the current to stick to the top plate of the cell.

As a result of this mechanism, the data show some scatter, which is more evident in the values of y_G than in those of K. This represents a novel feature for physically based self-similar solutions, which are generally expected to forget their initial conditions and

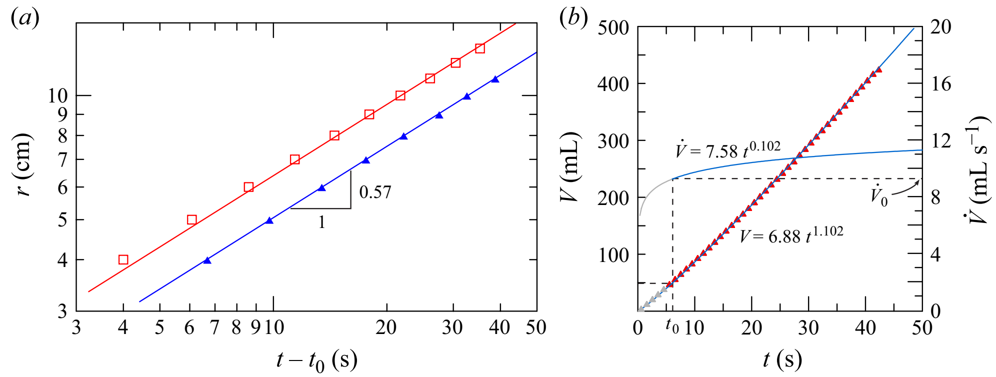

Figure 11. Experiment conducted with the same parameters as experiment 19, but featuring a delay of $t_0 \approx 6$ s in the fluid entering the cell. (*a*) Time series of front positions, grounding fronts are blue symbols and nose fronts are red symbols; and (*b*) delivered volume (symbols) and inflow rate (solid curve) over time.

approach intermediate asymptotics over time scales determined by the degree of deviation from idealised initial states.

The formation of the fountain suggests that during the initial phase, both the Froude number, defined as $Fr = U/\sqrt{gD}$, where U is the average velocity in the pipe and D is the inlet diameter, and the Weber number, defined as $We = \rho U^2 D/\Gamma$, plays a significant role. At $t = 1$ s, their values range from $Fr = 0.02$ to 0.20 and $We = 0.05$ to 5.3. Viscosity becomes the dominant factor only at a later stage. Enlarging the inlet diameter does not appear to be an effective solution to prevent dome formation during peak flow conditions. In fact, an overly large diameter can prevent the gravity current from initially adhering to the top plate of the cell, which is consistent with theoretical predictions, particularly for shear-thinning fluids injected with a waning flow rate.

Beyond this challenging effect, which requires careful consideration in the design of the experimental apparatus, the system nevertheless demonstrates a strong capacity to recover from initial and boundary conditions that differ from those assumed in the theoretical model.

Figure 11(*a*) illustrates the temporal evolution of the two fronts in an experiment conducted under the same conditions as experiment 19 (shear-thickening fluid with $n = 1.41$), except that the filling tube was not completely filled prior to the test; this resulted in a delay of $t_0 \approx 6$ s in flooding the cell, since the initial liquid volume first occupied the end of the tube. Figure 11(*b*) shows the inflow rate $\dot{V}$ and the volume of liquid delivered. Due to the delay, the initial flow rate was approximately $\dot{V}_0 = 9.1$ ml s^{-1}, higher than the initial zero flow rate observed in experiment 19, leading to an earlier formation of the grounding front. The volume missing in the gap was approximately 50 ml, almost 10 % of the total volume at the end of the test. Consequently, the actual value of $y_G = 0.79$ is significantly higher than the $y_G = 0.29$ estimated in experiment 19, although the coefficient K is slightly lower, indicating a slower nose; this reduction is attributed to the larger volume of fluid retained within the confined region of the gravity current. However, the time exponents $\beta_G = \beta_N = 0.57$ closely approximate the theoretical value 0.562. Physically, this suggests that beyond a brief initial transient governed by the second time scale t_0 shown in figure 11, the system rapidly settles into a new self-similar regime that retains the same exponents β_G, β_N as the solution described previously.

Figure 12 shows top view images of four experiments performed with a shear-thinning fluid advancing in a cell with a gap height of $H = 9.3$ mm. In three of these experiments,

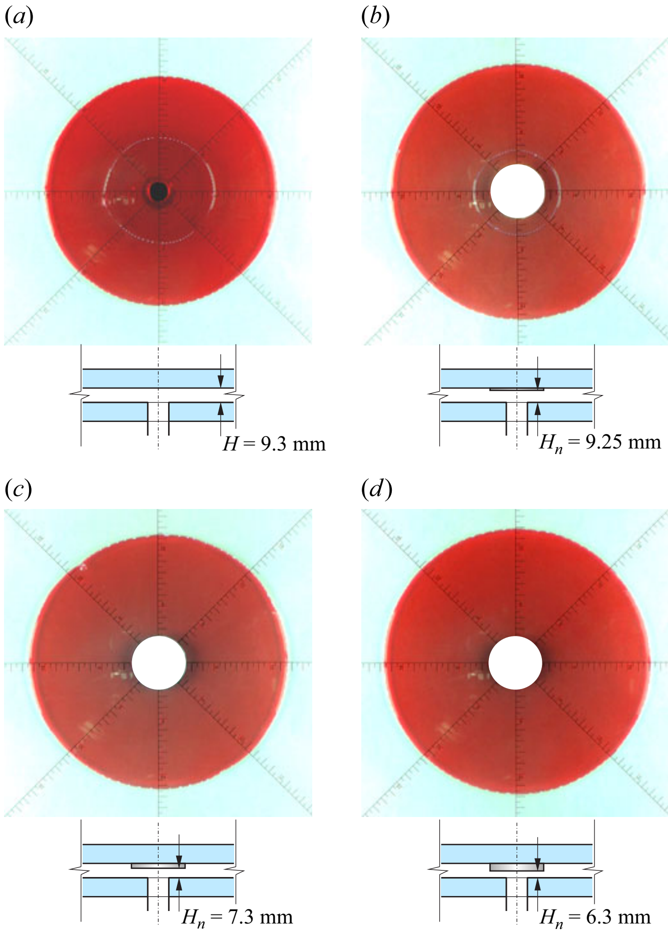

Figure 12. Experiments of gravity currents of a shear-thinning fluid for $H = 9.3$ mm, $J = 0.47$: (*a*) no nozzle; (*b*) nozzle with $H_n = 9.25$ mm; (*c*) nozzle with $H_n = 7.3$ mm; and (*d*) nozzle with $H_n = 6.3$ mm. All frames were captured at time $t = 23$ s.

a nozzle of varying thickness, formed by 5 cm diameter discs, was inserted to investigate the behaviour of the GC when contact with the top plate at the origin was prevented.

Upon comparing figures 12(*a*) and 12(*b*), it is evident that the presence of a layer 0.05 mm thick significantly affects the evolution of the GC, still resulting in the formation of a grounding front, although with a noticeable delay. As the thickness of the nozzle increases (corresponding to a decrease in H_n, figures 12*c* and 12*d*), the gravity current does not adhere to the top plate and instead evolves as an unconfined GC with a front speed that is largely independent of H_n.

5. Summary and conclusions

This study examined the gravity-driven flow of non-Newtonian fluids, theoretically schematised as power-law fluids, advancing within confined horizontal gaps, in axisymmetric cylindrical geometries. We performed 21 experiments in the three main rheological classes: shear-thinning, Newtonian and shear-thickening. The experimental propagation was compared with the predictions of a theoretical lubrication theory model which incorporates the surface tension effects on the grounding line through an effective parameter σ. The interesting physical feature is that the self-similar propagation pattern obtained for a system without surface tension ($\sigma = 0$) remains valid when the surface tension meniscus is significant ($\sigma > 0$). However, surface tension affects the position of the grounding line y_G and the propagation coefficient K. These results extend the previous work conducted only with Newtonian fluids in the same geometry (Hutchinson *et al.* 2023; Hutchinson 2024). All test fluids were thoroughly characterised in terms of density, surface tension and rheological parameters. To implement the required time-dependent volumetric inflow $\mathcal{V} = qt^{\alpha}$ determined by the non-unit exponent α, a PC-controlled syringe pump was used. This enabled the precise delivery of the waning flow rates for shear-thinning fluids, waxing flow rates for shear-thickening fluids and constant flow rates for Newtonian fluids (where $\alpha = 1$).

A distinctive feature of these partially confined gravity currents is the presence of two geometric scales: the first is the height of the gap H defining the degree of confinement, while the second corresponds to the unique intrinsic length scale that would govern an unconfined gravity current. This latter scale depends on the exponent α, the apparent viscosity ν and the flow rate coefficient q^*. For a generic value of α, a self-similar solution – characterised by synchronous propagation of the grounding line and the nose, together with a proportional growth of the unconfined portion – does not emerge. This behaviour is analogous to that observed in the study by Di Federico *et al.* (2017), where the introduction of the yield stress associated with the Herschel–Bulkley rheology introduced an additional geometric scale. In that case, self-similarity was recovered only for a specific value of the flow rate exponent, which aligned the yield-stress-induced length scale with the confinement scale defined by the gap width.

A further step, due to Hutchinson (2024) and Ungarish (2025*b*), involved identifying the presence of a capillary meniscus at the grounding line as the source of discrepancies between theory and experiments. In this framework, the additional geometric scale associated with the meniscus, whose exact shape is not well defined, is incorporated into the self-similar formulation by introducing a parameter that relates it to the height of the gap H; thus, preserving self-similarity. Our results are consistent with the suggestion of Hutchinson (2024) that the capillary number S is a fair approximation for σ. However, the ratio σ/S, as calculated on the basis of the values of σ and S listed in table 1, displays some scatter and, hence, the establishment of the exact correlation must be left for future work.

The experiments, which were characterised by particular complexity due to the need for precise measurements of rheometric parameters and surface tension, required several precautions. These included ensuring extreme cleanliness of all surfaces prior to injection of the fluid, carefully controlling the overall horizontality of the plates and modulating the flow rate increase function during the first few seconds of operation. This last precaution was necessary because, for experiments in which the volume inflow $\alpha < 1$ (corresponding to shear-thinning fluids) is constant, the expression of the theoretical flow rate involves time in the denominator, implying an initially infinite flow rate that is physically unattainable. To address this, a smooth interpolation function was used to gradually ramp the flow rate over the first 3 s, delivering the correct total volume without discontinuities. This issue does not arise for Newtonian fluids and shear-thickening fluids, for which $\alpha \geq 1$. However, we observed hysteresis effects – namely, the dependence of a system's state on its history – manifested through different current evolutions depending on the geometry of the flow inlet. Specifically, the presence of a nozzle with even a very slight reduction in the size of the gap, 0.5 % of the value H, causes a noticeable delay in the formation of the grounding line, which does not arise for larger reductions in the gap of the nozzle. This means that when the current has attached itself to the top plate, it remains there throughout its evolution. Otherwise, it evolves in the form of an unconfined current, contradicting the results of the theoretical model.

This sensitivity to initial conditions – arising from small perturbations induced by the inlet geometry – may seem at odds with the expected intermediate asymptotic behaviour of self-similar solutions, which are generally understood to 'forget' their initial conditions and evolve according to the dominant governing scales. For instance, while a lock release scenario is mathematically idealised as a Dirac delta function, experiments necessarily release a finite volume of fluid that occupies a finite domain at time $t = 0^-$. Despite this, the gravity current eventually evolves independently of this initial discrepancy, conforming to the theoretical self-similar solution.

Excluding surface tension effects, which influence whether the GC remains confined or becomes unconfined, an additional indication of the robustness of self-similar solutions lies in their persistence even when the inflow rate differs from the classical power-law form. In particular, we documented a case that involved delayed fluid injection under conditions similar to those of experiment 19: the GC still advanced in a self-similar manner, albeit with a different value of K.

Future research in this area may advance along three main avenues, either independently or in combination: (i) exploring more complex confinement geometries that better reflect subsurface conditions; (ii) incorporating rheological models beyond the power-law to capture more intricate non-Newtonian behaviours; and (iii) improving the simplified treatment of the capillary meniscus at the grounding line to a broader range of configurations.

Supplementary movies. Supplementary movies are available at https://doi.org/10.1017/jfm.2026.11677.

Funding. S.L. acknowledges that this work was supported by a Project funded under the National Recovery and Resilience Plan (NRRP), Mission 4 Component 2 Investment 1.5 – Call for tender No. 3277 of 30/12/2021 of Italian Ministry of University and Research funded by the European Union – NextGenerationEU. Project code ECS00000033, Concession Decree No. 1052 of 23/06/2022 adopted by the Italian Ministry of University and Research, CUP D93C22000460001, 'Ecosystem for Sustainable Transition in Emilia-Romagna' (Ecosister), Spoke 4. V.D.F. acknowledges partial support from Università di Bologna RFO (Ricerca Fondamentale Orientata) 2024.

Declaration of interests. The authors report no conflict of interest.

Appendix

The assessment of the relevant shear-rate interval is carried out separately for the free-surface region of the gravity current (GC) and for its confined region. For the free-surface configuration, we assume that the minimum shear rate occurs at the nose and can be approximated as $\dot{\gamma}_N = \dot{r}_N / l$, i.e. as the ratio between the instantaneous nose velocity (velocity scale) and the capillary length (length scale). For the confined GC, we assume that the extreme shear-rate values arise in the vicinity of the inlet and are given by $\dot{\gamma}_{r0} = Q/(2\pi r_0 H^2)$, where $r_0 = 1.25$ cm is the inlet radius, $Q/(2\pi r_0 H)$ defines the characteristic velocity scale and H is the characteristic length scale. Figure 13 presents the temporal evolution of both shear-rate estimates for all experiments.

Based on this, we adopt the corresponding shear-rate interval in figure 3 for interpolating the power-law model used to describe the fluid rheology.

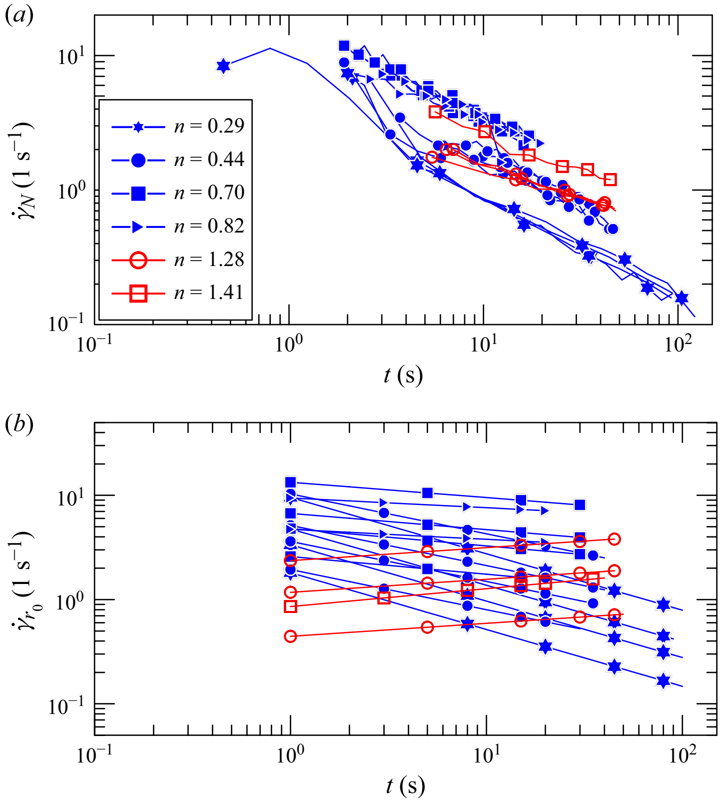

Figure 13. Diagrams illustrating the temporal evolution of the shear rate. (*a*) Shear rate at the nose, defined as $\dot{\gamma}_N = \dot{r}_N/l$; (*b*) shear rate at a radial position equal to the inlet tube radius, given by $\dot{\gamma}_{r_0} = Q/(2\pi r_0 H^2)$.

References

BARENBLATT, G.I. 1996 *Scaling, Self-similarity, and Intermediate Asymptotics: Dimensional Analysis and Intermediate Asymptotics*. Cambridge Texts in Applied Mathematics. Cambridge University Press.

BOYKO, E. & STONE, H.A. 2021 Flow rate–pressure drop relation for shear-thinning fluids in narrow channels: approximate solutions and comparison with experiments. *J. Fluid Mech.* **923**, R5.

DARBY, R. 1986 Laminar flow and turbulent pipe flows of non-Newtonian fluids. In *Encyclopedia of Fluid Mechanics* (ed. N.P. CHEREMISINOFF), vol. 7, pp. 19–53. Gulf Publishing Company Press.

DI FEDERICO, V., LONGO, S., KING, S.E., CHIAPPONI, L., PETROLO, D. & CIRIELLO, V. 2017 Gravity-driven flow of Herschel–Bulkley fluid in a fracture and in a 2D porous medium. *J. Fluid Mech.* **821**, 59–84.

DUDFIELD, P. & WOODS, A.W. 2014 On the periodic injection of fluid into, and its extraction from, a confined aquifer. *J. Fluid Mech.* **755**, 111–141.

FARCAS, A. & WOODS, A.W. 2015 Buoyancy-driven dispersion in a layered porous rock. *J. Fluid Mech.* **767**, 226–239.

GUNN, I. & WOODS, A.W. 2011 On the flow of buoyant fluid injected into a confined, inclined aquifer. *J. Fluid Mech.* **672**, 109–129.

GUO, B., ZHENG, Z., CELIA, M.A. & STONE, H.A. 2016 Axisymmetric flows from fluid injection into a confined porous medium. *Phys. Fluids* **28** (2), 022107.

HOFFMAN, D.A. 2014 Understanding the gravity of the situation: there are some mold-filling situations in which gravity indeed does have an effect. *Plast. Engng* **70** (10), 28–31.

HUTCHINSON, A.J. 2024 The effect of surface tension on axisymmetric confined viscous gravity currents. *Part. Differ. Equ. Appl. Math.* **12**, 100992.

HUTCHINSON, A.J., GUSINOW, R.J. & WORSTER, M.G. 2023 The evolution of a viscous gravity current in a confined geometry. *J. Fluid Mech.* **959**, A4.

Kistler, S.F. & Scriven, L.E. 1994 The teapot effect: sheet-forming flows with deflection, wetting and hysteresis. *J. Fluid Mech.* **263**, 19–62.

Longo, S., Di Federico, V., Archetti, R., Chiapponi, L., Ciriello, V. & Ungarish, M. 2013*a* On the axisymmetric spreading of non-Newtonian power-law gravity currents of time-dependent volume: an experimental and theoretical investigation focused on the inference of rheological parameters. *J. Non-Newton. Fluid Mech.* **201**, 69–79.

Mukherjee, P. & Balasubramanian, S. 2020 Energetics and mixing efficiency of lock-exchange gravity currents using simultaneous velocity and density fields. *Phys. Rev. Fluids* **5** (6), 063802.

Ng, C.-O. & Mei, C.C. 1994 Roll waves on a shallow layer of mud modelled as a power-law fluid. *J. Fluid Mech.* **263**, 151–184.

Nordbotten, J.M. & Celia, M.A. 2006 Similarity solutions for fluid injection into confined aquifers. *J. Fluid Mech.* **561**, 307–327.

Papadopoulos, C.E. & Yeung, H. 2001 Uncertainty estimation and Monte Carlo simulation method. *Flow Meas. Instrum.* **12** (4), 291–298.

Pegler, S.S., Maskell, A.S.D., Daniels, K.A. & Bickle, M.J. 2017 Fluid transport in geological reservoirs with background flow. *J. Fluid Mech.* **827**, 536–571.

Picchi, D., Ullmann, A., Brauner, N. & Poesio, P. 2021 Motion of a confined bubble in a shear-thinning liquid. *J. Fluid Mech.* **918**, A7.

Simpson, J.E. 1997 *Gravity Currents in the Environment and the Laboratory*. Cambridge University Press.

Taghavi, S.M., Seon, T., Martinez, D.M. & Frigaard, I.A. 2009 Buoyancy-dominated displacement flows in near-horizontal channels: the viscous limit. *J. Fluid Mech.* **639**, 1–35.

Ungarish, M. 2020 *Gravity Currents and Intrusions – Analysis and Prediction*. World Scientific.

Ungarish, M. 2025*a* Box model for confined power-law viscous gravity currents including surface tension effects. *Fluids* **10** (11), 1–22.

Ungarish, M. 2025*b* Self-similar flow of Newtonian and power-law viscous gravity currents in a confining gap in rectangular and axisymmetric geometries. *J. Fluid Mech.* **1007**, A4.

Yang, H. & Kowal, K.N. 2025 Non-porous viscous fingering of a thin film of fluid spreading over a lubricated substrate. *J. Fluid Mech.* **1013**, A32.

Zheng, Z., Christov, I.C. & Stone, H.A. 2014 Influence of heterogeneity on second-kind self-similar solutions for viscous gravity currents. *J. Fluid Mech.* **747**, 218–246.

Zheng, Z., Rongy, L. & Stone, H.A. 2015 Viscous fluid injection into a confined channel. *Phys. Fluids* **27** (6), 062105.

Zheng, Z. & Stone, H.A. 2022 The influence of boundaries on gravity currents and thin films: drainage, confinement, convergence, and deformation effects. *Ann. Rev. Fluid Mech.* **54**, 27–56.